Nanoscale

Accepted Manuscript

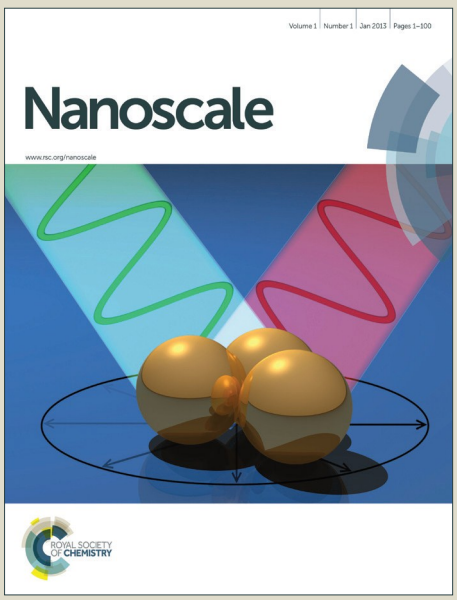

ROYAL SOCIETY OF CHEMISTRY

www.rsc.org/nanoscale

Predictive approach to CVD of crystalline layers of TMDs: The case of MoS_2

Kranthi Kumar V.[a], Sukanya Dhar[a], Tanushree H. Choudhury[b], S. A. Shivashankar[a] and Srinivasan Raghavan[a,b*]

[a]Centre for Nano Science and Engineering, [b]Materials Research Centre, Indian Institute of Science, Bangalore – 560012, India.

Abstract

Layered transition metal dichalcogenides (TMDs), such as MoS_2, are candidate materials for next generation 2-D electronic and optoelectronic devices. The ability to grow uniform, crystalline, atomic layers over large areas is the key to developing such technology. We report a chemical vapor deposition (CVD) technique which yields n-layered MoS_2 on a variety of substrates. A generic approach suitable to all TMDs, involving thermodynamic modeling to identify the appropriate CVD process window, and quantitative control of the vapor phase supersaturation, is demonstrated. All reactant sources in our method are outside the growth chamber, a significant improvement over vapor-based methods for atomic layers reported to date. The as-deposited layers are p-type, due to Mo deficiency, with field effect and Hall hole mobilities of up to 2.4 cm^2/V-s and 44 cm^2/V-sec respectively. These are among the best reported yet for CVD MoS_2.

* **Corresponding author E-mail:** sraghavan@cense.iisc.ernet.in

Keywords: MoS_2, chemical vapor deposition, thermodynamic modeling, supersaturation

1. Introduction

2-D or layered materials came into recent reckoning with the observation of ambipolar electric field effect in graphene flakes.[1,2] Following graphene,[3,4] a single sheet of carbon atoms, TMDs have emerged as a widely studied family of 2-D materials.[5,6] Given the diversity of their properties, ranging from semiconducting to metallic to superconducting,[7-9] the dichalcogenides or their combinations with layered conductors like graphene, or insulators like BN,[10] have already been explored for many novel hybrid electronic and optoelectronic devices.[11-13]

As with graphene, most initial research on dichalcogenides was confined to micron-sized flakes obtained by exfoliation from the bulk.[1,14,15] Such exfoliation is, however, not scalable. For integration of dichalcogenide-based devices into existing microelectronics technology, a CVD technique that allows controlled deposition of uniform layers over large areas, akin to that developed by Li et al. for graphene is required.[16] Currently, layers of MoS_2, the most widely studied dichalcogenide, have been obtained over large areas by sulfurization of evaporated MoO_3 [17-21] and $MoCl_5$,[22] dip-coated $(NH_4)_2MoS_4$,[23] sputtered Mo metal[24] and Mo-Au alloys.[25] Most of these efforts[17-24] involve vaporization of the starting materials within a reactor at fairly elevated temperatures of 500-900°C. This progress is significant as the structure of dichalcogenides is more complex than that of graphene rendering their nucleation and growth in the desired orientation more difficult.[19] However, technology integration requires a CVD method in which all precursors are introduced into the reactor in the gaseous form, from sources that can be vaporized externally at temperatures as low as possible. Although MoS_2 has been synthesized using vapor-transported $Mo(CO)_6$ [26] and $(NH_4)_2MoS_4$,[27] the end product did not consist of a controlled number of uniform layers over large areas. More importantly, hybrid devices such as those consisting of multiple

chalcogenides, graphene, and BN layers can also be synthesized in the same reactor without interruption or exposure to air, by the appropriate introduction of precursors. This would not be possible in the vapor transport processes, such as the ones previously mentioned, in which one of the precursors is always present in the reactor. [17-24]

We have developed a CVD process using $Mo(CO)_6$ and H_2S as precursors, which enables the uniform deposition of n-layered, n=1, 2, 3…>6, MoS_2 over large areas on a wide variety of substrates, including sapphire, oxidized silicon and fused quartz. The low boiling point of $Mo(CO)_6$ (156°C) and H_2S gas make these ideal precursors for CVD. Thermodynamic modeling was used to first deduce the growth window in which MoS_2 is the only solid phase formed. Kinetic control was then applied in this growth window by controlling supersaturation to obtain crystalline layers parallel to the substrate surface, as required for 2-D electronics. In the process developed, all precursors are brought into the vapor phase outside of the reactor at temperatures <100°C. This is not only critical to reducing nucleation and growth rates but also to the synthesis of doped device structures. A combination of thermodynamic modeling and kinetic control similar to that used in this study to deposit MoS_2 layers would be applicable to all TMDs of interest.

2. Experimental

2.1. Thermodynamic Modeling: A commercially available PC-based software program was used for the thermodynamic calculations [Autokumpu HSC Chemistry 6.1, Finland] carried out to identify the growth window.

2.2. Methods: $Mo(CO)_6$ (Sigma Aldrich (99.99%)) powder and H_2S (Bhoruka, 99.5%) gas were used for CVD growth of MoS_2 films. Growth was carried out in a custom-built

horizontal, hot-wall CVD reactor, shown in Fig. 1. The substrates, SiO_2/Si, c-plane sapphire, and fused quartz, were cleaned in acetone, isopropyl alcohol (IPA), and de-ionised (DI) water in an ultrasonic bath for 5 min each, and dried with UHP N_2 stream. $Mo(CO)_6$ powder was placed in a vaporizer and maintained at 25-130°C to obtain the required precursor concentration. To ensure complete transfer of the precursor in to the reactor, the vapor transport lines were maintained at the vaporizer temperature. Ar and H_2 were used as carrier gases, and H_2S as the reacting gas. To control the number of MoS_2 layers, the reactor pressure (P_{tot}) was maintained between 20 to 600 Torr. The growth temperature (T) was varied from 350°C to 850°C. To control the thickness of the layers formed, deposition duration (t) was varied from 10 s to 10 min. Prior to deposition, the reactor was pumped down to the desired pressure (P_{tot}), and the temperature was ramped at 25°C/min under a carrier gas flow of Ar and/or H_2 to the desired T and held for 15 min. The $Mo(CO)_6$ powder in the vaporizer is heated to the required temperature, maintaining a carrier gas flow of 15 sccm. The total pressure in the vaporizer is maintained at 20 psi, to achieve a flow of 1.8 sccm of $Mo(CO)_6$ into the reactor (detailed calculation is in supporting information). The ratios of gas flow rates, Mo:H_2S:(Ar or H_2), were maintained at 1:10:100 or 1:10:1000. After deposition, the films formed were sulfurized at the same T and P_{tot} for 10 min, with only H_2S flowing through the reactor.

2.3. Characterization and device fabrication: The samples were examined by optical microscopy (Leica) and field emission scanning electron microscopy (FESEM, Zeiss, Ultra 55) to check the uniformity of MoS_2 films deposited. Raman (Horiba, LabRam) spectra were used to determine the number and uniformity of layers. Atomic force microscopy (Bruker) was used to confirm the number of layers. The chemical composition was ascertained by x-ray photoelectron spectroscopy (Shimadzu, Axis Ultra DLD) (see supporting information for more details). The binding energies have been measured with respect to graphitic carbon at

284.5 eV. The crystallinity of the layers was examined by transmission electron microscopy (FEI, T20). For TEM and electrical characterization, MoS_2 layers were transferred onto a copper grid or a 500-nm-SiO_2/Si substrate, accordingly. For transferring onto a grid, a drop of IPA was placed on the substrate along with the grid. After the IPA is allowed to dry, the substrate was immersed in a HF solution (1:10), resulting in transfer of the MoS_2 layer onto the grid. For transferring onto a SiO_2/Si substrate, the sample was spin-coated with PMMA at 6000 rpm for 60 s. It was then baked at 150°C for 2 min. The sample was then immersed in HF solution (1:5) until the PMMA layer with MoS_2 detached from the underlying substrate. FETs were fabricated with 20 μm channel length (L) and 200 μm width (W) using photolithography. Source and drain pads of Cr/Au, 20/80 nm, were deposited by e-beam evaporation. 30 nm Al_2O_3 deposited by e-beam evaporation was used as the top gate oxide, with Cr/Au of 20/80 nm as the gate electrode. Hall measurements were carried out to determine mobility and carrier concentration.

3. Results and discussion

3.1. Thermodynamic modeling to determine growth window

By assuming the validity of equilibrium thermodynamics for the CVD process, "phase stability diagrams" can be determined, which can predict "process windows" for the deposition of the desired solid. The stability diagrams for the solid products of the reactant system of $Mo(CO)_6$-H_2S-Ar, for different temperatures (T) and reactant mixtures, obtained through thermodynamic calculations, are plotted in Fig. 1. The details of the thermodynamic calculations are provided in the supporting information, including the list of all the possible solid and gaseous products from the Mo-S-C-H-O system considered in the analysis (Table S1). All depositions for verifying the analytical results were carried out in the reactor shown

in Fig. 1a. Our thermodynamic modeling predicts that only MoS_2, carbon, and MoS_3 would be the solid phases formed. For a molar ratio of 10:1 between the precursors $Mo(CO)_6$ and H_2S, used for most of the growth conditions reported here, formation of MoS_3 is predicted at T<200°C. However, no deposition of MoS_3 was observed at these temperatures, as shown in Fig. S1. That the thermodynamically predicted formation of MoS_3 or MoS_2 at low temperatures is not experimentally observed is attributed to kinetic limitations. Raman peaks corresponding to MoS_2 were observed only at T>350°C. Subsequent discussion is therefore confined to depositions at T>350°C.

The ability of these phase diagrams in predicting growth outcomes is corroborated out by the Raman data from samples deposited over a range of temperatures for a particular pressure and gas composition. The phase diagram of Fig. 1b predicts that, with argon as carrier gas, the carbon content of the solid deposit decreases as the growth temperature (T) is raised. The Raman data, Fig. 1c, confirm this prediction, highlighting the importance of predictive modeling. On the other hand, the presence of minute residual amounts of carbon at 700°C - beyond the 575°C limit predicted by phase diagram - shows the need for experimental verification, as the accuracy of modeling is limited by the precision of the thermodynamic data available. At 850°C, there is "no trace" of carbon, and the presence of only MoS_2 is evidenced by the Raman spectrum.

Total reactor pressure, P_{tot}, is one of the most important CVD parameters. An optimal choice of P_{tot}, as will be seen later, was critical in controlling MoS_2 layer deposition in this study. Thermodynamic modeling, Fig. 1d, predicts that, for a given T, an increase in P_{tot} leads to an increase in the carbon content of the solid phase. Raman spectra (Fig. S2-a) of deposited samples confirm this trend. The corresponding phase stability diagram at P_{tot} = 600 Torr, the

upper bound used in our studies, is included in the supporting information, Fig. S3. Modeling predicts (Fig. 2a), however, that, at a given T, the deposition of carbon at high P_{tot} can be precluded by using a mixture of argon and hydrogen as the carrier gas (as is common in CVD). Carbon content can be reduced by increasing the partial pressure of hydrogen. Indeed, in pure H_2 ambient, carbon is predicted to be absent at all T when P_{tot}>10 Torr (Fig. 2b). This prediction is confirmed by the Raman data in Fig. 2c and Fig. S2-b. The ability to predict the completely different outcomes on using Ar versus Ar+H_2 mixtures as carrier gas highlights the importance of such thermodynamic modeling.

3. 2. Growth of few-layered to mono-layered MoS_2 by kinetic control

To obtain monolayered or few-layered MoS_2 films predictably and with precision, kinetic control, within the thermodynamic window, is called for and may be exercised through variation of supersaturation. Under conditions wherein thermodynamic modeling predicts the formation of pure MoS_2, the gas phase supersaturation, or ΔG for the chemical reaction, Equation 1, was calculated using Equation 2.

$$Mo(CO)_6 + 2H_2S \longrightarrow MoS_2 + 6CO + 2H_2 \quad (1)$$

$$\Delta G = RT \ln\left(\frac{\eta_{Mo(CO)_6}\eta_{H_2S}^2\eta_{tot}^5}{\eta_{CO}^6\eta_{H_2}^2P_{tot}^5K_{Eq}}\right) \quad (2)$$

where $P_{tot,}$ is the total reactor pressure in atmospheres, T the growth temperature and η, the flow rates of various gases as indicated by the subscripts. K_{Eq} calculated from standard data is listed in the supporting information. A decrease in ΔG was affected by reducing precursor fluxes suitably and increasing the total pressure (Equation 2). The effect of this reduction is tabulated in the supporting information, Table S2. The ΔG values would be a maximum at the

zero-point in the reactor (Fig. 1a), and would decrease along the length of the reactor. According to Equation 2, lower temperatures would result in reduced supersaturation. However, the Raman data in Fig. 1c and 2c show that MoS_2 films deposited at 500°C have a larger full-width at half maximum (FWHM) than films deposited at 850°C. A similar trend is also observed at higher pressure as shown in Fig. S2b. As larger FWHM is indicative of a more defective film, the depositions were carried out at 850°C. P_{tot} being the only independent variable parameter in the logarithmic term in Equation 2, it is a critical parameter for reducing ΔG. At P_{tot} = 20 Torr, the largest ΔG values used in our study, bulk MoS_2 was obtained in 10 minutes everywhere in the reactor. The effect of reduction in ΔG by increasing P_{tot} from 20 Torr to 850 Torr, in the thermodynamically permissible window at 850°C, spanning the duration of growth (t) is shown in Fig. 3. The reduction in supersaturation achieved by this increase in P_{tot} was 175 kJ/mol as calculated from Equation 2. The details of the calculations are provided in the supporting information. As summarized in Fig. 3, by the SEM, AFM, optical and spectroscopic information, a combined reduction in ΔG and t resulted in uniform, controlled deposition of MoS_2 from bulk-like to 6 layers to a monolayer. The number of layers obtained for the identical growth conditions was the same for sapphire, SiO_2/Si and quartz. For a combination of the smallest ΔG and t, growth was slowed down well enough to yield discrete hexagonal islands. To put the supersaturation concerned in perspective, we estimate that the large islands demonstrated by recent PVT reports using bulk MoS_2 as the source were obtained with a ΔG of ~131 kJ/mol(see supporting information). Typical durations required to obtain a full monolayer by PVT is of the order of 20 minutes,[28] versus 1 minute in the present study. This indicates that the actual supersaturation values in the CVD here are much higher. While equipment limitation prevents us from achieving even lower supersaturations currently, the present work shows that, with a further reduction in ΔG and hence in nucleation rates, CVD would eventually

yield islands as large as those obtained by PVT. For instance, Equation 2 shows that this could be done by going to even higher total pressures. Fig. 3a provides SEM images of MoS_2 films ranging from few layers to islands 25 μm in size. MoS_2 grains and complete monolayer grown at 850 Torr (850°C) for various growth times are shown in Fig. S4. The reduction in FWHM of the Raman spectra shows the improvement in quality. Fig. 3b shows the topography and step height obtained by AFM of crystalline MoS_2 from few-layers to 1L. The step height of 1L is around 0.75 to 0.77 nm, consistent with previously reported values of 0.72 to 1 nm.[22,29] The step height of 2L and 3L is ~1.55 nm and ~2.4 nm, respectively. The AFM images of MoS_2 on other substrates are shown in Fig. S5. The Raman spectra of MoS_2, layers are shown in Fig. 3c, along with that of exfoliated bulk MoS_2 (MoS_2>6 layers which has been exfoliated using scotch tape) as reference. As the layer thickness decreases, the interlayer coupling decreases, reducing the gap between E^1_{2g} and A_{1g}. The difference is 18.9 cm^{-1}, 21.8 cm^{-1}, 22.3 cm^{-1} and 27 cm^{-1} for 1L, 2L, 3L and bulk exfoliated MoS_2, respectively.[22,29-31] Fig. 3d shows variation in the Raman peak separation and position with the number of layers. It is evident that, as thickness increases, the in-plane mode E^1_{2g} red-shifts and A_{1g} mode blue-shifts. The peak separation also increases with thickness, but equalizes for films thicker than 6L. Details about the variation in the FWHM of the peaks with growth conditions are given in Fig. S6. PL spectra, which provide another indication of the number of layers, are shown in Fig. 3e for the MoS_2 layers grown on sapphire. The two prominent peaks around 627 nm and 667 nm correspond to A1 and B1 direct excitonic transitions. The strength of the PL signal is in the order 1L>2L>3L, with bulk MoS_2 yielding a negligible PL signal. This reaffirms that the bandgap (E_g) in MoS_2 changes from direct to indirect, as layer thickness increases. The peaks undergo a red-shift with increasing thickness, highlighting a reduction in E_g, as expected.[32-33]

Uniform deposition over large areas, for different layers, is illustrated in Fig. 4a, which shows photographs of MoS_2 on 1 cm x 1 cm sapphire substrates. The variation in the Raman spectra and the FWHM of monolayer MoS_2 on different substrates is shown in Fig. 4b. The FWHM of the films deposited on the substrates (E^1_{2g} : 3.1-3.6 cm^{-1} and A_{1g} : 5.1-5.3 cm^{-1}) is higher than that of exfoliated single layer MoS_2 (E^1_{2g} : 2.8 cm^{-1} and A_{1g} : 4.7 cm^{-1}). The variation in the FWHM for the substrates SiO_2/Si, sapphire and quartz is however not very significant, indicating that layers are of comparable quality, irrespective of the substrate. These FWHM are comparable with PVT grown monolayer values E^1_{2g} : 3.5 cm^{-1} and A_{1g} : 6.6 cm^{-1}.[18] Fig. 4d-e shows the uniformity in coverage on sapphire substrate through Raman mapping of monolayer MoS_2 over a 100 μm x 100 μm scan area. The peak separation is in the range of 18.5 to 20 cm^{-1}. These values concur with a previous report on monolayer MoS_2.[22] The Raman spectra and mapping data for triangular islands of MoS_2 on SiO_2/Si and monolayer films on diverse substrates are given in Fig. S7-10. Uniformity over entire 1 cm^2 sapphire is shown in Fig. S8.

The crystalline structure of the grown layers wa investigated by TEM. Fig. 5a shows a low-magnification image of a monolayer grown on SiO_2/Si at 500 Torr at 850°C. The high-resolution image (Fig. 5b) shows the hexagonal ordering present at the atomic scale. The inset in Fig. 5b highlights the single-crystalline diffraction pattern obtained. The chemical composition of the deposited layers was ascertained by XPS analysis. Fig. 5c shows the spectra obtained from 3L films as-deposited. The Mo spectra show evidence of the presence of Mo^{4+}, corresponding to MoS_2, and Mo^{6+}, corresponding to MoO_3. The formation of MoO_3 is attributable to the oxidation outside the CVD chamber - of metallic Mo arising either from incomplete sulfurization or from the partial reduction of the deposited MoS_2 while being cooled in H_2 ambient. When the MoS_2 films are annealed post growth in a H_2S ambient for

10 min and cooled in the same ambient, only the peak corresponding to Mo^{4+} is seen in the XPS spectrum (Fig. 5d) The sulfurization step is thus crucial to achieving the "right" chemical composition. After sulfurization, the Mo:S ratio is 0.8:2, indicating Mo deficiency. This ratio calculated for MoS_2 >3L(detailed growth conditions in Table S2) also gave similar results. The Mo error bar is 0.82±0.08 for 3L(5 samples), 0.85±0.09 for 4L(5 samples) and 0.79±0.06 for 5L(2 samples). This Mo deficiency, as discussed in the next section, results in p-type behavior of the as-grown films. For reference purposes, bulk exfoliated MoS_2 sample was also characterised by XPS (see Fig. S11). The calculated atomic concentration of Mo:S was 1:1.912 thereby implying it should be n-type behavior. Device characterstics, see Fig. S11, indicate that this is indeed so. This exercise thus serves as an internal calibration of our XPS data and shows that the correlation with device behaviour is consistent. Most data in the literature, except in one report,[24] concern n-type MoS_2.[34-38] The ability to vary stoichiometry by varying the vapor phase composition is one of the strengths of CVD and is very important for obtaining p- and n-type layers for device applications.

Preliminary electrical characterization of the CVD MoS_2 - field effect transistors (FET) fabricated both in top-gate and bottom-gate configurations also confirm the Mo deficiency shown by XPS. Fig. 6a is a schematic representation of a such a MoS_2 FET. Fig. 6b shows the output characteristics of the device and Fig. 6c shows transfer characteristics of a 20 μm channel-length device. The top-gate characteristics are in the inset. The linear output characteristics for a low drain voltage indicate good ohmic contact at the source and drain pads. The transfer characteristics of the MoS_2 device show the aforementioned p-type behaviour. The field effect mobility of the charge carriers is extracted from the slope of the linear regime, using Equation 3

$$\mu = \left(\frac{\partial I_{ds}}{\partial V_g} \right) \frac{L}{W C_{ox} V_{ds}} \quad (3)$$

where L is the channel length, W the channel width, and C_{OX} the gate capacitance.

It is observed that on-off ratios for the trilayer MoS_2 device is around 10^5, with an estimated mobility of 2.4 $cm^2V^{-1}s^{-1}$ in the bottom-gate configuration, and ~7.1 $cm^2V^{-1}s^{-1}$ in the top-gate configuration. Fig. 6d summarizes the mobility obtained from FETs with MoS_2 of differing number of layers, including electron mobility of exfoliated bulk MoS_2. The mobility is seen to decrease with the increase in layer number. This is contrary to reported literature trends.[34-38] The layers used for the electrical characterization were grown under different supersaturations(details in Table S2). For instance, 6 layered MoS_2 has been grown under higher supersaturation than 3 layered MoS_2. As a result, the grain size in these films are also different. FWHM of these layers, given in Figure S6, shows that with increasing layer numbers, crystallinity degrades. Consequently, we believe that the precise mechanism of mobility degradation originates from defect scattering as indicated by the reduction in crystallinity. As suggested by the results in this paper, even better layers can be achieved by tuning the physico-chemical parameters during growth. Hall measurements, which are independent of contact resistance were also performed(included in the supporting information), confirms p-type behavior. A carrier concentration of 3 x 10^{16} cm^{-3} and a mobility of 44 cm^2/V-sec was measured on 3L samples. These Hall mobilities are among the highest reported for p-type MoS_2. (in Table S4 of supporting information). The low hole concentrations point to a deep acceptor level introduced by Mo vacancies. Our calculations (see supporting information) indicate that this level should lie at 0.62 eV above the valence band edge in reasonable agreement with theoretical estimates which point to their being at 1 eV.[39]

4. Conclusions

In summary, a CVD technique compatible with traditional device integration has been developed to deposit MoS_2 atomic layers over large areas using $Mo(CO)_6$ and H_2S. Thermodynamic modeling has been used to deduce the growth window most conducive to the deposition of pure MoS_2. Control of supersaturation within this growth window was critical to obtaining uniform layers of the desired thickness, from discrete crystalline islands to monolayers to films >6 layers. The layers deposited have been investigated by Raman spectroscopy, XPS, AFM and TEM to ascertain the number of layers, their uniformity and crystallinity. Monolayers of MoS_2 grown at lower supersaturation have single-crystalline domains as large as 25 μm. The layers are p-type, due to Mo deficiency. Field effect and Hall hole mobilities of up to 2.4 cm^2/V-s and 44 cm^2/V-sec respectively were measured at a carrier concentration of $3x10^{16}$ /cm^3.

ACKNOWLEDGEMENTS

The authors would also like to acknowledge the Department of Science and Technology, Government of India for the financial support under the Grant No SR/S2/CMP-02/2007, SR/S3/ME/045/2007, SR/WOS-A/CS-69/2012 and the TUE project for nanoscience and technology. The authors would like to acknowledge the National Nanofabrication Center (NNfC), Micro and Nano Characterization Facility (MNCF) and the Advanced Facility for Microscopy and Microanalysis (AFMM) for the fabrication and characterization work done. I would like to thank Prof. Navakanta Bhat, CeNSE IISc for his suggestions.

SUPPORTING INFORMATION

Methodology for thermodynamic modeling, supersaturation calculation, Raman, optical microscopy and AFM analysis of MoS_2 single layers are available in the supporting information.

REFERENCES

1 K. S. Novoselov, A. K. Geim, S. V. Morozov, D. Jiang, Y. Zhang, S. V. Dubonos, I. V. Grigorieva and A. A. Firsov, *Science,* 2004, **306** , 666–669.

2 K. S. Novoselov, D. Jiang, F. Schedin, T. J. Booth, V. V. Khotkevich, S. V. Morozov and A. K. Geim, *Proc. Natl. Acad. Sci. United States Am.*, 2005, **102** , 10451–10453.

3 A. K. Geim, *Science,* 2009, **324**, 1530–1534.

4 A. K. Geim and K. S. Novoselov, *Nat. Mater.*, 2007, **6**, 183–191.

5 M. Chhowalla, H. S. Shin, G. Eda, L. J. Li, K. P. Loh and H. Zhang, *Nat. Chem.*, 2013, **5**, 263–275.

6 S. Z. Butler, S. M. Hollen, L. Cao, Y. Cui, J. A. Gupta, H. R. Gutiérrez, T. F. Heinz, S. S. Hong, J. Huang, A. F. Ismach, E. Johnston-Halperin, M. Kuno, V. V Plashnitsa, R. D. Robinson, R. S. Ruoff, S. Salahuddin, J. Shan, L. Shi, M. G. Spencer, M. Terrones, W. Windl and J. E. Goldberger, *ACS Nano,* 2013, **7**, 2898–2926.

7 K. K. Kam and B. A. Parkinson, *J. Phys. Chem.*, 1982, ***86***, 463–467.

8 J. A. Wilson and A. D. Yoffe, *Adv. Phys.*, 1969, **18**, 193–335.

9 A. H. Castro Neto, *Phys. Rev. Lett.*, 2001, **86**, 4382–4385.

10 C. R. Dean, A. F. Young,I. Meric,C. Lee, L. Wang, S. Sorgenfrei, K. Watanabe, T. Taniguchi, P. Kim, K. L. Shepard and J. Hone, *Nat. Nanotehnol.*, 2010, **5**, 722–726.

11 Z. Liu, L. Ma, G. Shi, W. Zhou, Y. Gong, S. Lei, X. Yang, J. Zhang, J. Yu, K. P. Hackenberg, A. Babakhani, J. C. Idrobo, R. Vajtai, J. Lou and P. M. Ajayan, *Nat. Nanotechnol.*, 2013, **8**, 119–124.

12 W. J. Yu, Y. Liu, H. Zhou, A. Yin, Z. Li, Y. Huang and X. Duan, *Nat. Nanotechnol.*, 2013, **8**, 952-958.

13 K. Roy, M. Padmanabhan, S. Goswami, T. P. Sai, G. Ramalingam, S. Raghavan and A. Ghosh, *Nat. Nanotechnol.*, 2013, **8**, 826–830.

14 J. N. Coleman, M. Lotya, A. O'Neill, S. D. Bergin, P. J. King, U. Khan, K. Young, A. Gaucher, S. De, R. J. Smith, I. V Shvets, S. K. Arora, G. Stanton, H. Y. Kim, K. Lee, G. T. Kim, G. S. Duesberg, T. Hallam, J. J. Boland, J. J. Wang, J. F. Donegan, J. C. Grunlan, G. Moriarty, A. Shmeliov, R. J. Nicholls, J. M. Perkins, E. M. Grieveson, K. Theuwissen, D. W. McComb, P. D. Nellist and V. Nicolosi, *Science*, 2011, **331** , 568–571.

15 H. S. S. Ramakrishna Matte, A. Gomathi, A. K. Manna, D. J. Late, R. Datta, S. K. Pati and C. N. R. Rao, *Angew. Chemie Int. Ed.*, 2010, **49**, 4059–4062.

16 X. Li, W. Cai, J. An, S. Kim, J. Nah, D. Yang, R. Piner, A. Velamakanni, I. Jung, E. Tutuc, S. K. Banerjee, L. Colombo and R. S. Ruoff, *Science*, 2009, **324** , 1312–1314.

17 X. Wang, H. Feng, Y. Wu and L. Jiao, *J. Am. Chem. Soc.*, 2013, **135**, 5304–5307.

18 Y. H. Lee, X. Q. Zhang, W. Zhang, M. T. Chang, C. T. Lin, K. D. Chang, Y. C. Yu, J. T. W. Wang, C. S. Chang, L. J. Li and T. W. Lin, *Adv. Mater.*, 2012, **24**, 2320–2325.

19 S. Najmaei, Z. Liu, W. Zhou, X. Zou, G. Shi, S. Lei, B. I. Yakobson, J. C. Idrobo, P. M. Ajayan and J. Lou, *Nat. Mater.*, 2013, **12**, 754–759.

20 Y. Cheng, K. Yao, Y. Yang, L. Li, Y. Yao, Q. Wang, X. Zhang, Y. Han and U. Schwingenschlogl, *RSC Adv.*, 2013, **3**, 17287–17293.

21 Y. C. Lin, W. Zhang, J. K. Huang, K. K. Liu, Y. H. Lee, C. T. Liang, C. W. Chu and L. J. Li, *Nanoscale*, 2012, **4**, 6637–6641.

22 Y. Yu, C. Li, Y. Liu, L. Su, Y. Zhang and L. Cao, *Sci. Rep.*, 2013, **3**.

23 K. K. Liu, W. Zhang, Y. H. Lee, Y. C. Lin, M. T. Chang, C. Y. Su, C. S. Chang, H. Li, Y. Shi, H. Zhang, C. S. Lai and L. J. Li, *Nano Lett.*, 2012, **12**, 1538–1544.

24 Y. Zhan, Z. Liu, S. Najmaei, P. M. Ajayan and J. Lou, *Small*, 2012, **8**, 966–971.

25 I. Song, C. Park, M. Hong, J. Baik, H. J. Shin and H. C. Choi, *Angew. Chemie Int. Ed.*, 2014, **53**, 1266–1269.

26 M. R. Close, J. L. Petersen, E. L. Kugler and W. Virginia, *Inorg. Chem.*, 1999, **38**, 1535–1542.

27 Y. Shi, W. Zhou, A. Y. Lu, W. Fang, Y. H. Lee, A. L. Hsu, S. M. Kim, K. K. Kim, H. Y. Yang, L. J. Li, J. C. Idrobo and J. Kong, *Nano Lett.*, 2012, **12**, 2784–2791.

28 S. Wu, C. Huang, G. Aivazian, J. S. Ross, D. H. Cobden and X. Xu, *ACS Nano,* 2013, **7**, 2768–2772.

29 C. Lee, H. Yan, L. E. Brus, T. F. Heinz, J. Hone and S. Ryu, *ACS Nano,* 2010, **4**, 2695–2700.

30 H. Li, Q. Zhang, C. C. R. Yap, B. K. Tay, T. H. T. Edwin, A. Olivier and D. Baillargeat, *Adv. Funct. Mater.,* 2012, **22**, 1385–1390.

31 A. Molina-Sánchez and L. Wirtz, *Phys. Rev. B,* 2011, **84**, 155413.

32 A. Splendiani, L. Sun, Y. Zhang, T. Li, J. Kim, C. Y. Chim, G. Galli and F. Wang, *Nano Lett.,* 2010, **10**, 1271–1275.

33 K. F. Mak, C. Lee, J. Hone, J. Shan and T. F. Heinz, *Phys. Rev. Lett.,* 2010, **105**, 136805.

34 K. Gacem, M. Boukhicha, Z. Chen and A. Shukla, *Nanotechnology,* 2012, **23**, 505709.

35 Z. Yin, H. Li, H. Li, L. Jiang, Y. Shi, Y. Sun, G. Lu, Q. Zhang, X. Chen and H. Zhang, *ACS Nano,* 2011, **6**, 74–80.

36 B. Radisavljevic, A. Radenovic, J. Brivio, V. Giacometti and A. Kis, *Nat. Nanotechnol.,* 2011, **6**, 147–150.

37 A. M. van der Zande, P. Y. Huang, D. A. Chenet, T. C. Berkelbach, Y. You, G. H. Lee, T. F. Heinz, D. R. Reichman, D. A. Muller and J. C. Hone, *Nat. Mater.,* 2013, **12**, 554–561.

38 W. Wu, D. De, S. C. Chang, Y. Wang, H. Peng, J. Bao and S. S. Pei, *Appl. Phys. Lett.*, 2013, **102**, 142106.

39 J. F. Noh, H. Kim, Y. S. Kim, *Phys. Rev. B*, 2014, **89**, 205417.

Figure captions

Fig. 1 CVD phase stability in Ar ambient (a) Schematic representation of the CVD system used for the synthesis of MoS_2 (b) Calculated stability windows for various condensed phases at P_{tot} = 20 Torr. (c) Raman spectra (with exfoliated bulk MoS_2 as reference) of multilayer MoS_2 films deposited in argon ambient on sapphire over a wide range of T, with P_{tot} = 20 Torr and $Mo(CO)_6$:H_2S = 1:10 with indices in bracket showing FWHM of corresponding E^1_{2g} and A_{1g} peaks. (d) Contour plot showing the variation in the mole percentage of MoS_2 in the MoS_2-C film at different temperatures and pressures for the composition represented by the dotted line in (b). The colored dots in (b) and (d) correspond to Raman spectra in (c) of samples 1, 2, 3 and 4 deposited at different temperatures.

Fig. 2 CVD phase stability in Ar/H_2 and H_2 ambient (a) Contour plot showing the formation of MoS_2 and C, at P_{tot} = 20 torr, when the Ar:H_2 ratio is changed from 75:25 to 0:100 with $Mo(CO)_6$:H_2S = 1:10. (b) The contour plot for the formation of MoS_2 and C in H_2 ambient, as a function of T and P_{tot}. (c) Raman spectra (with exfoliated bulk MoS_2 as reference) of multilayer MoS_2 films deposited on sapphire in H_2 ambient over a wide range of T, keeping P_{tot} = 20 Torr and $Mo(CO)_6$:H_2S = 1:10. The indices in bracket show FWHM of corresponding E^1_{2g} and A_{1g} peaks. The colored dots in (b) correspond to Raman spectra in (c) of samples 1, 2 and 3 deposited at different temperatures. As predicted carbon(G) is absent.

Fig. 3 Few-layers to monolayer through supersaturation control (a) SEM images of MoS_2, from few to monolayer, deposited in hydrogen ambient at 850^{o}C, by varying supersaturation. The P_{tot} which controls the supersaturation for given flux, and growth duration (t) are indicated. (b) AFM images, with superimposed line scan, showing MoS_2 films, from three-

layered (3L) to a monolayer (1L). (Scale bar corresponds to 2 μm) (c) Raman spectra of MoS_2 films, from 1L to 6L, together with that of exfoliated bulk MoS_2 (d) The variation in the peak separation and position of the Raman spectra, as a function of the number of layers (e) The PL spectra of MoS_2 films as the number of layers L increases, showing the change from direct to indirect band gap for large L.

Fig. 4 Uniformity of the deposited layers. (a) Photograph of MoS_2 films with different L, grown on sapphire substrate. The color is an indication of the number of layers grown. (b) Raman spectra of MoS_2 monolayers on various substrates along with their FWHM. The Raman spectra of exfoliated monolayer and bulk MoS_2 is also included (c) Optical image of single layer of MoS_2 grown on sapphire, with a 100 μm x 100 μm area selected for mapping of the (d) E^1_{2g} mode (e) A_{1g} mode and (f) peak difference. The mapping highlights the uniformity in layer thickness.

Fig. 5 Structural and chemical analysis of MoS_2 layers grown at 850°C by TEM and XPS. (a) Low- magnification image of a monolayer. (b) High-resolution image of a monolayer. The inset shows the characteristic single crystalline pattern, with hexagonal symmetry. XPS spectra of MoS_2 films 3L grown at 20 Torr, before (c) and after (d) sulphurization is presented. The Mo 3d spectrum obtained before sulphurization shows the presence of Mo^{6+}, corresponding to MoO_3, which is absent after sulphurization.

Fig. 6 Electrical characterization of MoS_2 MOSFETs. (a) Schematic representation of a dual-gate MoS_2 FET transistor. (b) Output characteristics of the device. (c) Transfer characteristics of a device with 20 μm channel length, with the bottom-gate configuration. The top-gate characteristics are shown as an inset. (d) Mobility as a function of the number of layers.

Figure 1.

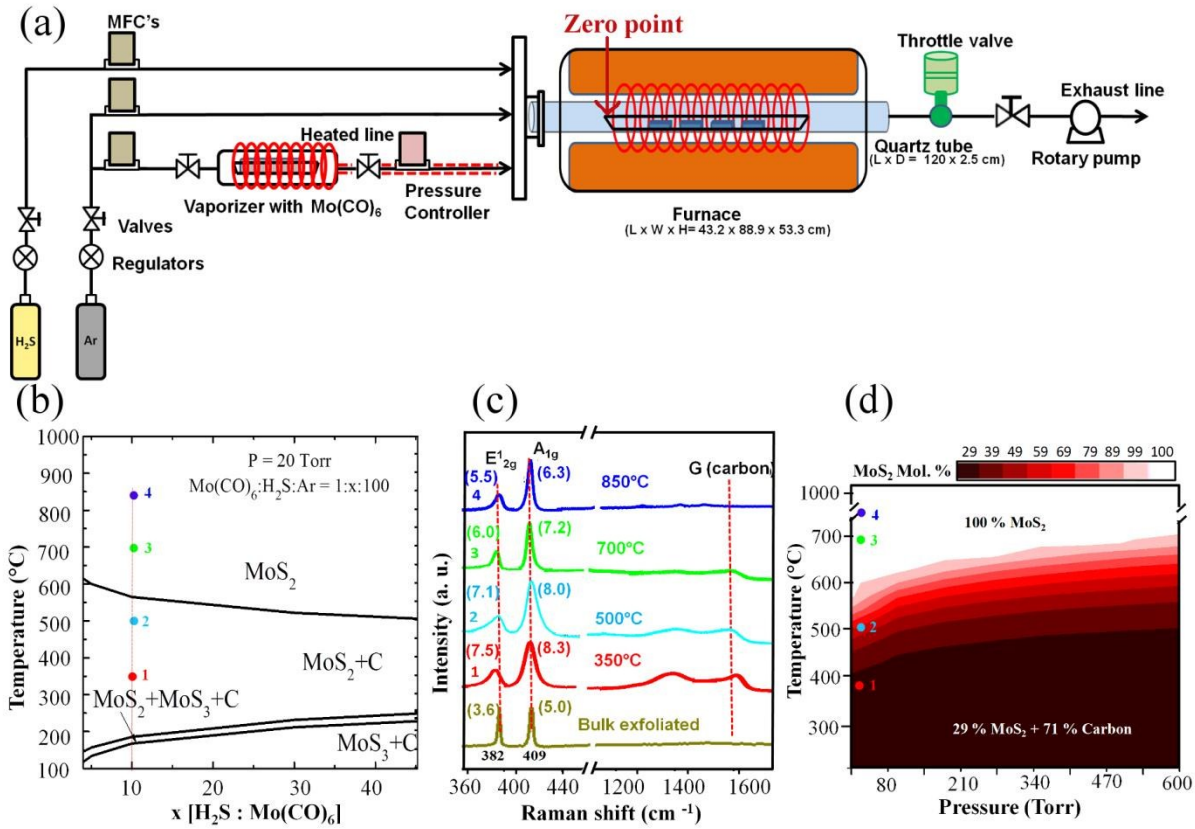

Figure 2.

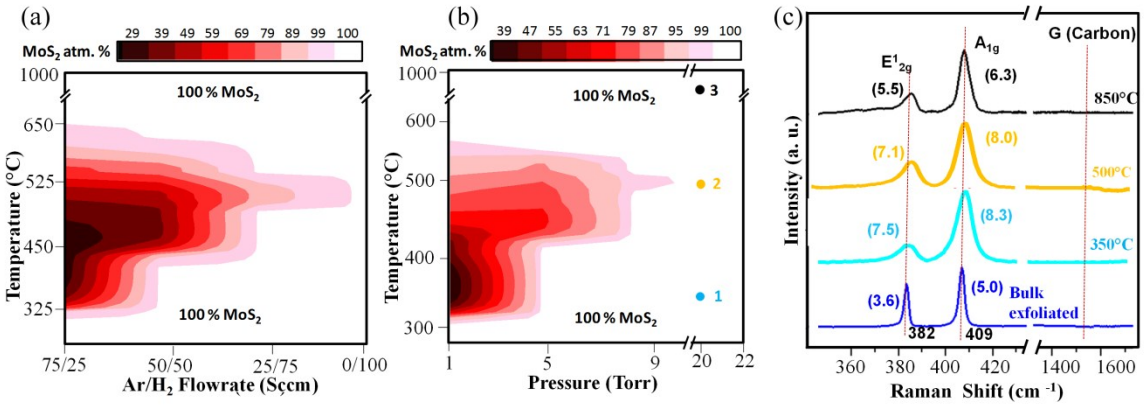

Figure 3.

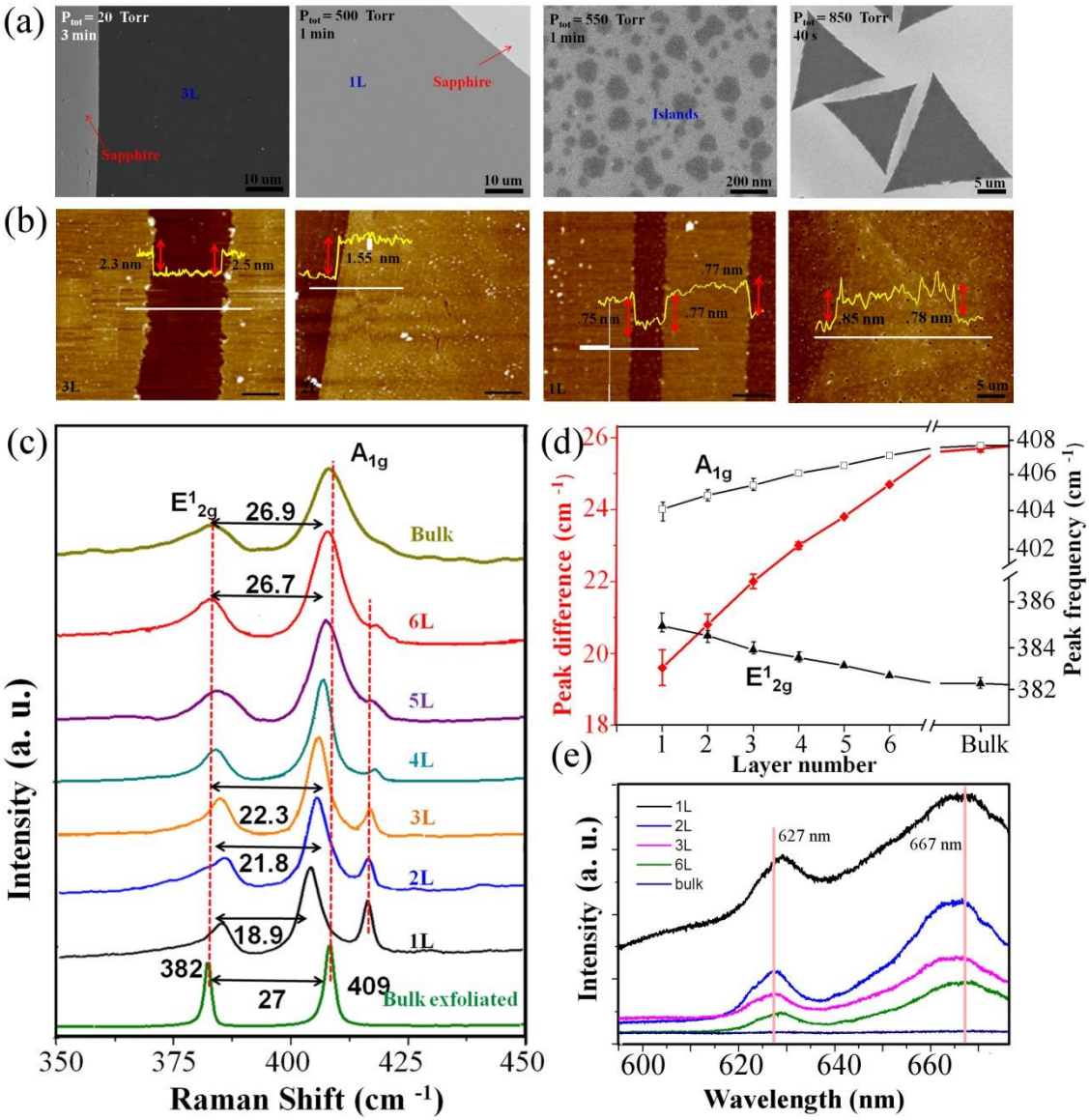

Figure 4.

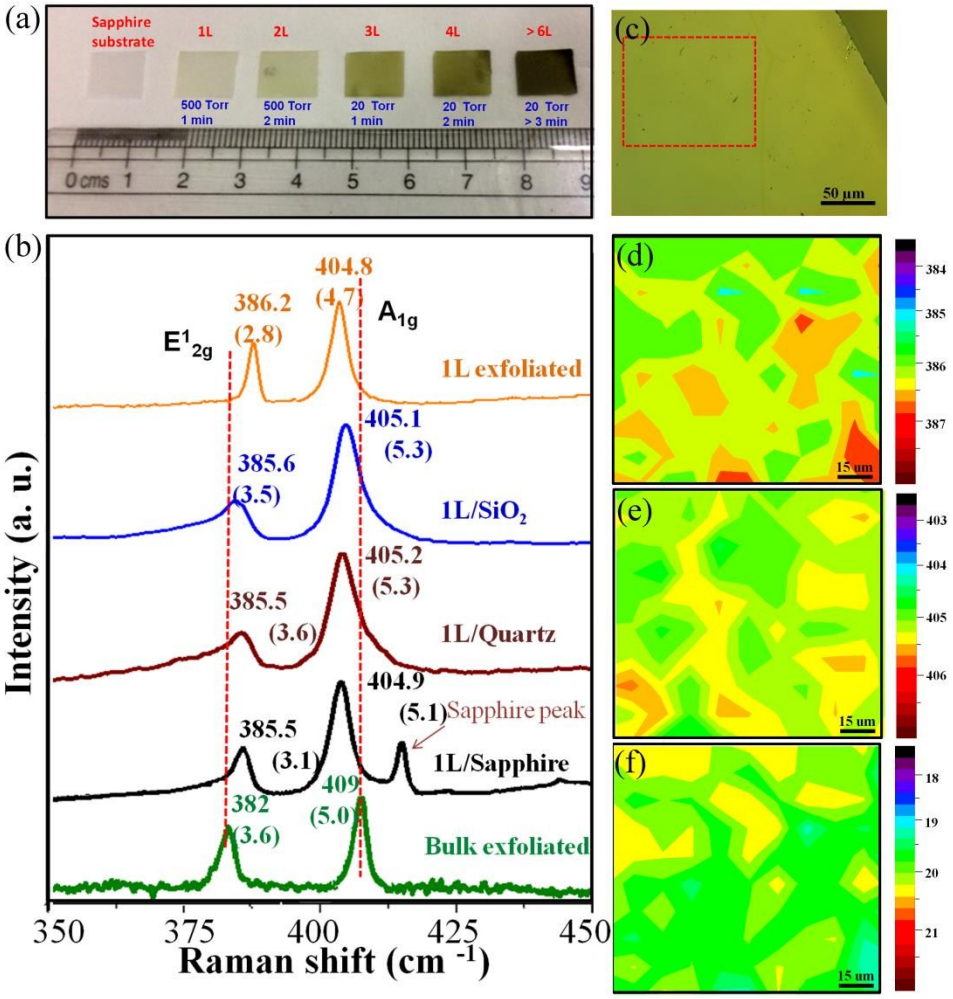

Figure 5.

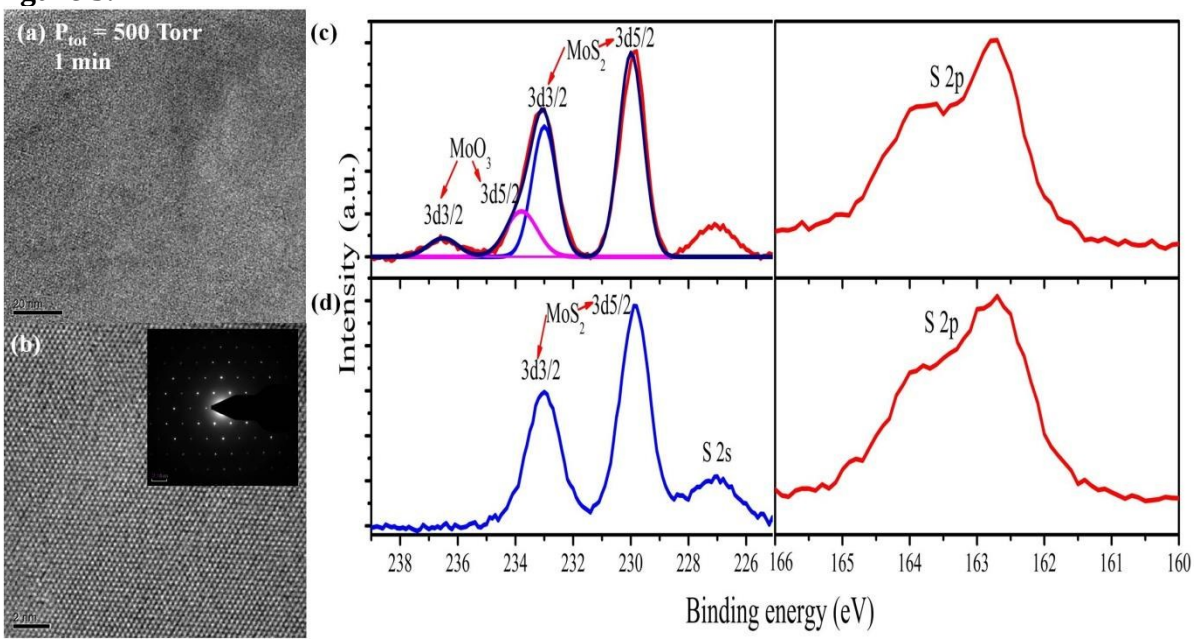

Figure 6.

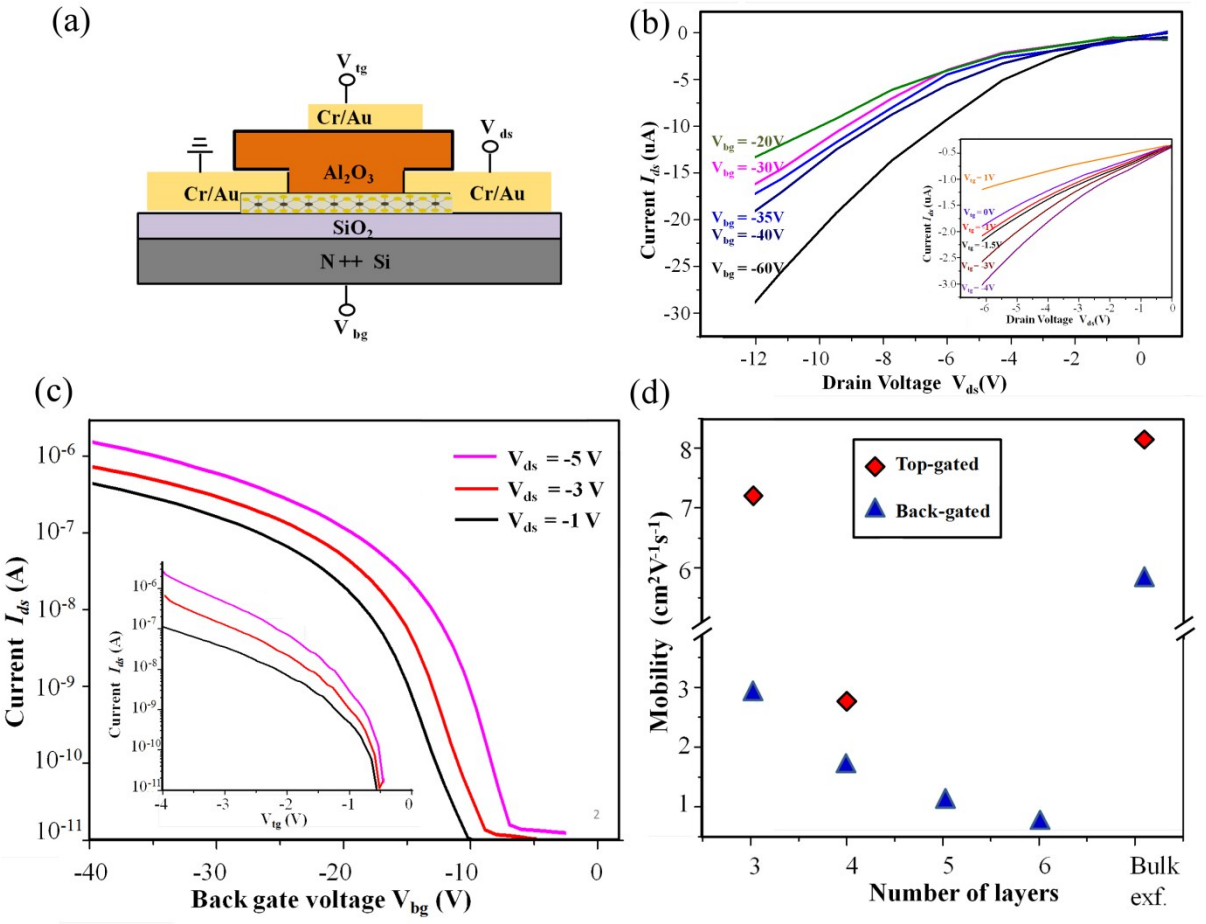

Table of Contents entry image:

A generic approach suitable to all transition metal dicalchogenides has been demonstrated. Thermodynamic modeling has been used to identify the appropriate CVD process window. The growth has been controlled by tuning the vapor phase supersaturation. As as result MoS_2 growth from bulk to monolayers has been acheived.